Chapter 10
Extension of the Monogenic Phasor Method to Extract Displacements and Their Derivatives from 3-D Fringe Patterns

C. A. Sciammarella and L. Lamberti

Abstract Determination of displacement field and its derivatives from fringe patterns entails four steps: (1) information inscription; (2) data recovery; (3) data processing; (4) data analysis. Phase retrieval and processing are very important in fringe analysis. In [1], these steps were discussed for 1D signals, introducing a 2D abstract space as phase evaluation requires a vectorial function. The Hilbert transform allows to obtain signal in-quadrature defining local phase. A 3D abstract space must be generated to handle the analysis of 2D signals and simultaneously extend Hilbert transform to 2D. The theory of a monogenic function introduced in [2] is elaborated here: the 3D vector in a Cartesian complex space is graphically represented by a Poincare sphere. This provides a generalization of the Hilbert transform to a 2D version of the Riesz transform, a modified version of that described in [2]. Theoretical derivations are supported by actual application of theory and corresponding algorithms to 2D fringe patterns and by comparing obtained results with literature.

Keywords 2D signals • Displacements and strains of 3D solid bodies • Poincare hyper-sphere • Heart tissue deformation

10.1 Introduction

In preceding papers [1, 2], the process of extracting displacement information and its derivatives has been analyzed from the point of view of application of the Image Analysis Science basic framework. Fringe pattern analysis is a sub discipline of the above-mentioned science that is applied to a mathematical model of the kinematics of the continuum. Fringe pattern analysis is also applied in the metrology of bodies. Both fields of deformation analysis and metrology information gathering have many common aspects but the 3D metrology of objects requires the utilization of many additional resources of the Image Analysis Science than the analysis of deformations. This paper will be limited to the analysis of deformations of 3D solids. In [1, 2], a new approach to fringe patterns analysis was introduced. For historic reasons, methods of displacement information determination have been associated with developments of techniques that utilize different approaches to generate and decode signals containing displacement information. Apart from the pathways of different methods, the same basic science is behind the utilized approaches and the same basic rules and restrictions apply to all of them.

10.2 Determination of the Displacement Field in 3D

The first step in generating displacement data in 3D is to have a carrier on the volume under observation. A carrier is a known signal that upon deformation of the analyzed body will be modified from a certain known configuration, called the reference configuration or base configuration, to another configuration, the deformed configuration. The displacement information may be extracted from a deterministic signal or from a random signal. The basic methodology is the same, the random signal introduces additional challenges and difficulties but does not modify the process of extracting the displacement

C.A. Sciammarella (✉)
Department of Mechanical, Materials and Aerospace Engineering, Illinois Institute of Technology, 10 SW 32nd St, 60616, Chicago, IL, USA
e-mail: sciammarella@iit.edu

L. Lamberti
Dipartimento Meccanica, Matematica e Management, Politecnico di Bari, Viale Japigia 182, 70126, Bari, Italy

L. Lamberti et al. (eds.), *Advancement of Optical Methods in Experimental Mechanics, Volume 3*,
Conference Proceedings of the Society for Experimental Mechanics Series, DOI 10.1007/978-3-319-63028-1_10

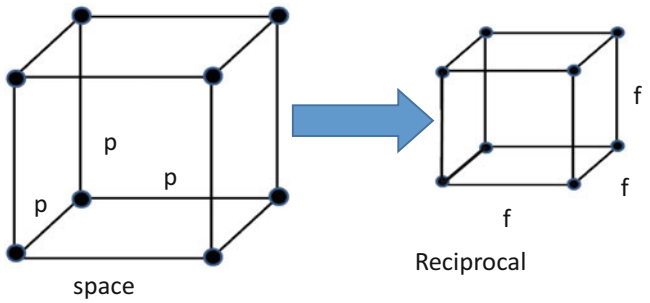

Fig. 10.1 Physical space tagged with planes separated by the pitch p and reciprocal frequency space with plane distances f

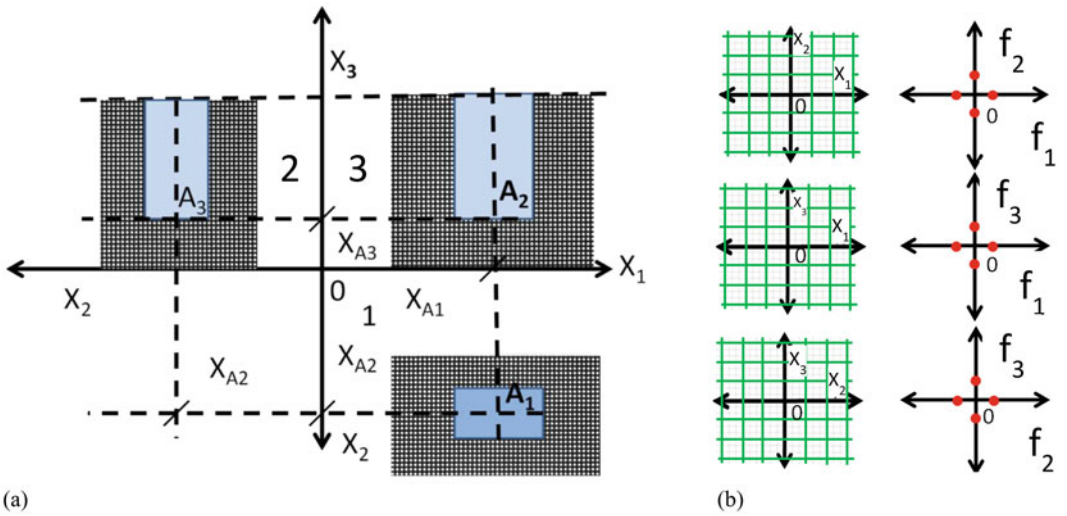

Fig. 10.2 A prismatic body tagged with a 3D system of planes; (**a**) Descriptive geometry: 3 quadrants represent sections of the body; (**b**) cross sections of the coordinate planes in space and frequency

information. Let us outline the basic process of extracting 3-D information utilizing deterministic signals. The relationship between p and f is,

$$f = \frac{1}{p} \tag{10.1}$$

Figure 10.1 shows the physical space tagged with planes separated by the pitch p, spatial distance between planes that define the voxels containing the volume information. Corresponding to the voxels in the physical space there are voxels in the reciprocal space or frequency space with plane distances f.

Figure 10.2 provides a 3D scheme for spatial and frequency analysis of displacements and the corresponding derivatives. At this point, it is not necessary to specify how the reference system is introduced to the medium under analysis. There are several alternative procedures that can be utilized. The reference system is associated with a Cartesian system of coordinates.

Figure 10.2 illustrates a tagged 3D body utilizing Descriptive Geometry representation. The planes cover the whole volume, Fig. 10.2a. Figure 10.2b shows an enlarged view of the cross sections set of planes corresponding to the voxels that will carry the displacement information and the dots that define in the frequency space the family of orthogonal lines corresponding to these planes.

The coordinate system X_1, X_2 and X_3 is a Lagrangian or material system of reference. The Eulerian system of reference x_1, x_2 and x_3 is selected with planes parallel to the Lagrangian system. To keep the developments very general, large deformations are included, one of the problems that arise is to compare the very different geometries generated in the process of deformation.

Figure 10.3 shows the displacement vector of a voxel and its projections in the coordinate system.

Figure 10.4 illustrates the process of large deformation of a vessel recorded in a time sequence; time $t = 0$ corresponds to the reference configuration. A parameter must be introduced to connect different stages of the process of deformation,

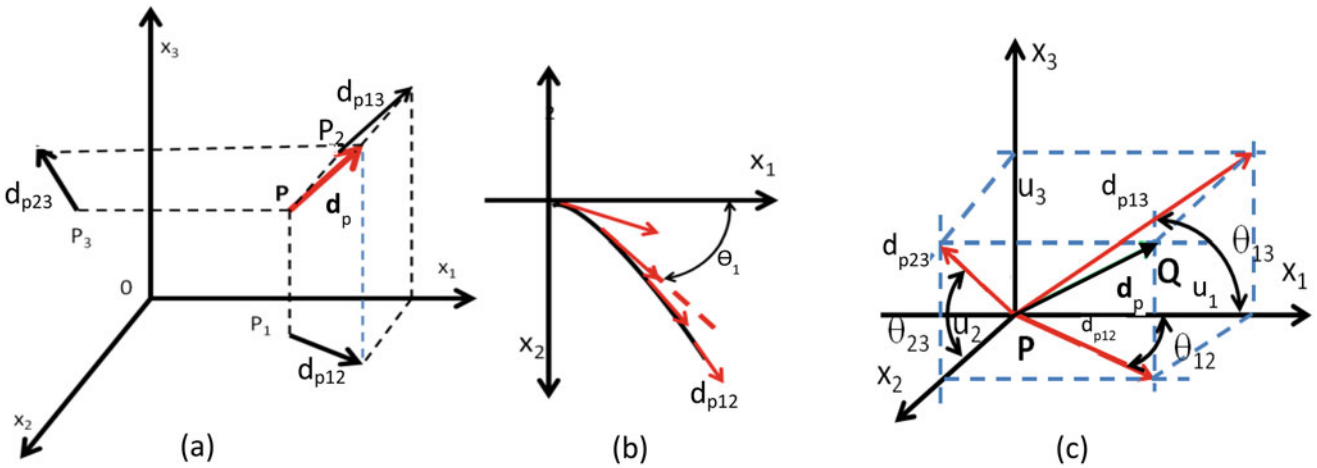

Fig. 10.3 (**a**) Displacement vector $\mathbf{d_p}$ in the 3-D space; (**b**) projections of the displacement vector in the plane x_1-x_2, at successive times; (**c**) projections of the vector d_p and corresponding angles

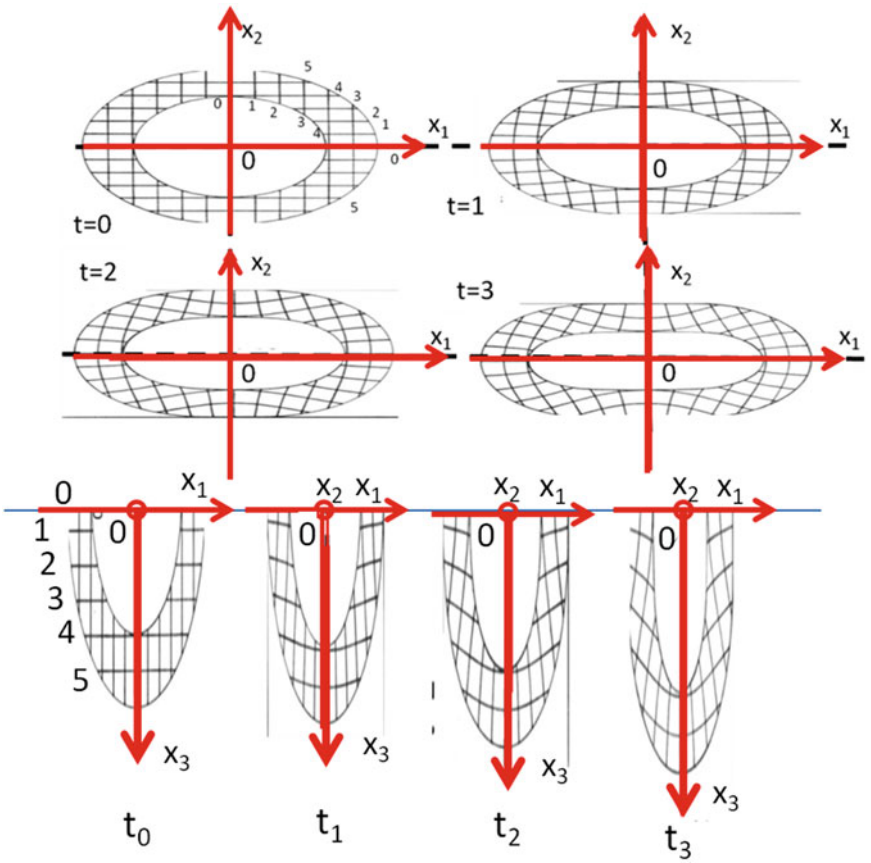

Fig. 10.4 Large deformations of a vessel taken in a time sequence. Time t = 0 corresponds to the reference configuration

in this example, the time t corresponding to different recordings. Because the planes are fixed to the body's material, the correspondence among volume elements can be obtained due to the parametrization of the planes with orders that are preserved in the deformation course. A matter of notation, we consider real- or complex-valued functions $f(\mathbf{x})$ defined on $\Re_n$, where n is an orderly list of integers. Ordinary case letters will represent scalar quantities, bold letters will represent vectorial quantities and we will write $f(\mathbf{x})$ or $f(x_1,...,x_n)$, the bold lower case indicating a vector quantity or we will list the low cases variables whichever is more convenient in context. The following notation will be utilized, $f_i(\mathbf{x})$ are functions of $\mathbf{x}$ and the index "i" will take the values, i = 1,2,3.

Equation (10.2) gives the displacement vector of a point P of the continuum shown in Fig. 10.3, in a Cartesian system of axes,

$$\mathbf{d_p} = u_1 e_1 + u_2 e_2 + u_3 e_3 \tag{10.2}$$

where e_1,e_2, e_3 are the versors of the coordinate system.

The projected vectors in each reference plane are given by,

$$\mathbf{d}_{p12} = u_1\ e_1 + u_2\ e_2 \tag{10.3}$$

$$\mathbf{d}_{p13} = u_1\ e_1 + u_3\ e_3 \tag{10.4}$$

$$\mathbf{d}_{p23} = u_2\ e_2 + u_3\ e_3 \tag{10.5}$$

It is necessary to connect the displacement vector to the signal carrier of displacement information a scalar that represents light intensities in terms of gray levels. This is done through the equation,

$$d_{pij}(x) = \frac{\phi_i(x)}{2\pi} p \tag{10.6}$$

where $\phi_i(\mathbf{x})$ is the local phase, the ratio $\frac{\varphi_i(x)}{2\pi} = n$ is the fringe order. Since we are speaking of local fringe orders, n will be a real number $n \leq 0, 1$. p is the signal pitch. Equation (10.6) is the transformation scale between the intensities and the displacements. Hence, one can write

$$\begin{cases} \|d_{p12}\| = \frac{\|\phi_{12}\|}{2\pi} p \\ \|d_{p13}\| = \frac{\|\phi_{13}\|}{2\pi} p \\ \|d_{p23}\| = \frac{\|\phi_{23}\|}{2\pi} p \end{cases} \tag{10.7}$$

For a generic point P the resultant vector is the sum of three components vectors,

$$\mathbf{d_p}\,(x, t) = \left[\mathbf{d_{p12}}\,(x_1, x_2, t) + \mathbf{d_{p23}}\,(x_2, x_3, t) + \mathbf{d_{p13}}\,(x_1, x_3, t)\right] \tag{10.8}$$

It can be observed in Fig. 10.3 that the third component $\mathbf{d_{p23}}$ is determined if the other two components are known.

The angle that the projected vector $\mathbf{d_{p12}}$ makes with axis x_1 is,

$$\theta_{12} = \text{arctg}\frac{u_2}{u_1} \tag{10.9}$$

Similar equations can be written for θ_{13} and θ_{23}.

To proceed with the determination of the components of the displacement vector it is necessary to review some of the properties of the Fourier transform, FT, that also apply to the Hilbert transform.

10.3 Properties of the Fourier Transform

The recovery of the displacement information is done working with recorded patterns of gray levels (scalar quantities) that result from the modulation of sinusoidal carriers, hence in the following analysis the utilized variables are light intensities I(**x**). In the derivation presented in this section, the multidimensional FT is applied, a generalization of the 1D to multiple spaces that deals with vectorial quantities [3, 4]. While gray levels are scalars, after the FT is applied to gray levels, one gets vector quantities, intensity vectors corresponding to the projection of the displacement vector along a selected coordinate axis. In [2], it was shown that the Fourier transform and the Hilbert transform can be utilized as two possible alternatives to decode displacements from recorded fringe patterns. In this paper, to generalize the procedures derived in [1, 2], we will utilize the FT; similar arguments could be derived applying the generalized Hilbert transform.

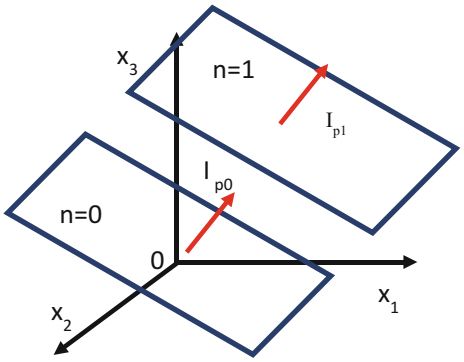

Fig. 10.5 Planes in the 3D and projected displacement vectors

Let us consider the 3D case, the following equations for the FT applies,

$$\hat{f}\,(\xi_1,\xi_2,\xi_3) = \mathrm{F}\left[\mathrm{f}\,(\mathrm{x}_1,\mathrm{x}_2,\mathrm{x}_3)\right] = \int_{-\infty}^{\infty}\int_{-\infty}^{\infty}\int_{-\infty}^{\infty} \mathrm{e}^{-2\pi i\,(x_1\xi_1+x_2\xi_2+x_3\xi_3)}\mathrm{f}\,(\mathrm{x}_1,\mathrm{x}_2,\mathrm{x}_3)\,\mathrm{dx}_1\mathrm{dx}_2\mathrm{dx}_3 \tag{10.10}$$

If we consider the exponent of the exponential function in (10.10), this exponent equals 1 whenever $\mathbf{x}\cdot\boldsymbol{\xi}$ is an integer, that is, when

$$\mathrm{x}_1\xi_1 + \mathrm{x}_2\xi_2 + \mathrm{x}_3\xi_3 = \mathrm{n} \tag{10.11}$$

Equation (10.11) corresponds to the tangent planes to a family of curved surfaces that correspond to the tagging planes shown in Fig. 10.3 and that after deformations have become curved surfaces. These curved surfaces are the equivalent in 3D to the isothetic lines in 2D that locally can be represented by the tangent planes shown in Fig. 10.5. Equation (10.11) represents the orthogonal normal vectors to the 3D isothetic surfaces.

It can be shown that the modulus of the intensity light vector is given by,

$$\|I_p\| = \frac{1}{\sqrt{\xi_1^2+\xi_2^2+\xi_3^2}} \tag{10.12}$$

where,

$$\|\xi\| = \sqrt{\xi_1^2+\xi_2^2+\xi_3^2} \tag{10.13}$$

$\boldsymbol{\xi}$ is the corresponding frequency vector in the frequency space illustrated in Fig. 10.1.

The exponent of Eq. (10.10) can be written,

$$\mathrm{e}^{-2\pi i\,(\,x_1\xi_1+x_2\xi_2+x_3\xi_3)} = \mathrm{e}^{-2\pi i x_1\xi_1}\;e^{-2\pi i x_2\xi_2}\;e^{-2\pi i x_3\xi_3} \tag{10.14}$$

Each of the three exponential terms is of the form $\cos\phi + i\sin\phi$;, and the corresponding frequencies are ξ_i, (i = 1,2 3). The first exponential term varies along x_1 with a frequency ξ_1, likewise the other two terms respectively vary along x_2, x_3 with frequencies ξ_2 and ξ_3. This implies three separate transforms along the three axes x_i.

The above expression gives the relationship between the vector representing the signal in 3D and its projections in the Cartesian coordinates versors $\mathbf{e_i}$, (i = 1,2 3). Figure 10.6 represents the 3D vector $\mathbf{I}_p(\mathbf{x})$.

The modulus of this vector is,

$$\|I_p\| = \sqrt{\mathrm{I}_1^2+\mathrm{I}_2^2+\mathrm{I}_3^2} = \frac{1}{\sqrt{\xi_1^2+\xi_2^2+\xi_3^2}} \tag{10.15}$$

$\mathbf{I}_p$ is the 3D normal vector of the curved surfaces that provide the 3D space equivalent of the 2D isothetic lines. In the 2D case, the projected displacement vector remains in the 2D plane and has components along the x_1 and the x_2 axes. In the 3D case, the projected displacement vector has components along x_1, x_2 and x_3, Fig. 10.6.

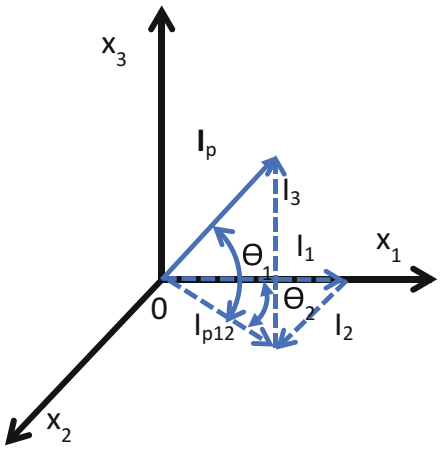

Fig. 10.6 Resultant projected vector in the 3-D space

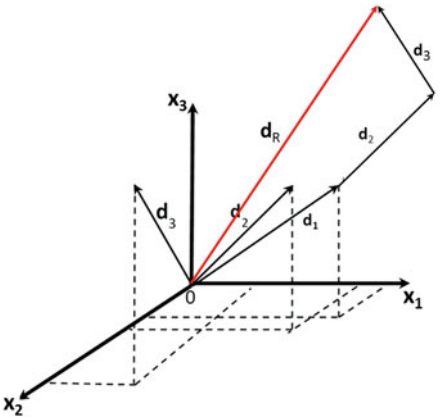

Fig. 10.7 Vector displacement at a voxel obtained as a sum of the vectors of the family of three tagging planes

From Fig. 10.6 one obtains the relationships between the vector $\boldsymbol{I}_p$ and its projections,

$$\mathrm{I}_1 = \mathbf{I}_p \cos\ \theta_1\ \cos\ \theta_2 \tag{10.16}$$

$$\mathrm{I}_2 = \mathbf{I}_p \cos\ \theta_1\ \sin\ \theta_2 \tag{10.17}$$

$$\mathrm{I}_3 = \mathbf{I}_p \sin\ \theta_1 \tag{10.18}$$

Equations (10.16) to (10.18) give the relationship between the vector $\boldsymbol{I}_p$ and its projections in the Cartesian coordinates of versors $\boldsymbol{e_i}$, (i=1,2 3).

Calling vector $\boldsymbol{I_{p1}}$ one of the three projection vectors ($\boldsymbol{I_{p1}}$, $\boldsymbol{I_{p2}}$ and $\boldsymbol{I_{p3}}$), that correspond to the three families of tagging planes, the resultant vector is given by the vectorial equation,

$$\boldsymbol{I}_{pT}\,(\boldsymbol{x}) = \boldsymbol{I}_{p1}\,(\boldsymbol{x}) + \boldsymbol{I}_{p2}\,(\boldsymbol{x}) + \boldsymbol{I}_{p3}\,(\boldsymbol{x}) \tag{10.19}$$

For each tagging plane with normal n_i, there is a vector $\boldsymbol{I_{pi}}$. The vectorial equation (10.19) provides the vector sum. Then, one has three projection equations for each one of the components of the light intensity vectors $\boldsymbol{I_{pi}}\,(\boldsymbol{x})$,

$$I_{pT}\,(\boldsymbol{x}) = \left[I_{p11} + I_{p12} + I_{p13}\right]\boldsymbol{e_1} + \left[I_{p11} + I_{p12} + I_{p13}\right]\boldsymbol{e_2} + \left[I_{p11} + I_{p12} + I_{p13}\right]\boldsymbol{e_3} \tag{10.20}$$

These resultant intensity vectors are converted into projected displacements vectors through the application of the theory of complex signals. Equation (10.20) is graphically represented in Fig. 10.7.

10.4 Derivation of the 4D Hyper-Sphere

One can generalize the equivalent of the Poincare sphere in the 3D complex space [2] by resorting to a 4D complex space. The 4D expression for a hyper-sphere of radius $R = I_{sp}$ in the complex space is given by the 4D complex vector,

$$\vec{\vec{I}}_{sp} = \begin{bmatrix} I_1 \\ I_2 \\ I_3 \\ I_4 \end{bmatrix} \tag{10.21}$$

where the modulus of $\vec{\vec{I}}_{sp}$ is given by,

$$\left\| \vec{\vec{I}}_{sp} \right\| = I_{sp} = \sqrt{I_1^2 + I_2^2 + I_3^2 + I_4^2} = R^2 \tag{10.22}$$

The components of the vector are,

$$I_1 = I_{sp} \cos\phi \, \cos\theta_1 \, \cos\theta_2 \tag{10.23}$$

$$I_2 = I_{sp} \cos\phi \, \cos\theta_1 \, \sin\theta_2 \tag{10.24}$$

$$I_3 = I_{sp} \cos\phi \, \sin\theta_1 \tag{10.25}$$

$$I_4 = I_{sp} \sin\phi \tag{10.26}$$

Figure 10.8 illustrates the relationship between the vector I_p and the vector I_{sp} in the complex plane. Equation (10.15) provides I_p.

From Eq. (10.2),

$$\left\| \mathbf{d}_p(x) \right\| = \sqrt{u_1^2(x_1) + u_2^2(x_2) + u_3^2(x_3)} \tag{10.27}$$

Calling d_p, the modulus of $\boldsymbol{d}_p$ and the local phase ϕ, from Eq. (10.6) it follows,

$$\phi = \frac{2\pi d_p}{p} \tag{10.28}$$

From Fig. 10.8,

$$I_{sp} = \frac{I_p}{\cos\phi} \tag{10.29}$$

Then one has obtained all the elements of the complex vector $\vec{\vec{\mathbf{I}}}_{\mathbf{sp}}$.

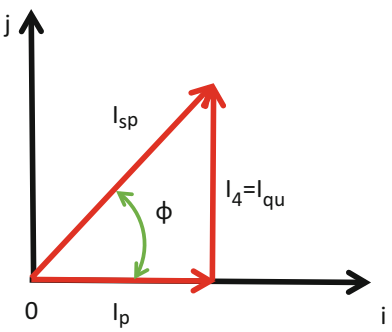

Fig. 10.8 Determination of I_4 in the complex plane

10.5 Computation of the Derivatives of the Displacements

In [5], it is mentioned that there are four fundamental tensors that can be utilized in Continuum Mechanics to define different forms of strain tensors and the corresponding definitions are given. The tensors are denoted in the literature as [F], [G], the inverse $[F]^{-1}$ and [J]. It is necessary to address a problem that occurs when it is not feasible to get all the system of tagging planes indicated in Figs. 10.1 and 10.4.

$$[J] = \begin{bmatrix} \frac{\partial u_1}{\partial x_1} & \frac{\partial u_1}{\partial x_2} & \frac{\partial u_1}{\partial x_3} \\ \frac{\partial u_2}{\partial x_1} & \frac{\partial u_2}{\partial x_2} & \frac{\partial u_2}{\partial x_3} \\ \frac{\partial u_3}{\partial x_1} & \frac{\partial u_3}{\partial x_2} & \frac{\partial u_3}{\partial x_3} \end{bmatrix} \tag{10.30}$$

Equation (10.30) gives the derivatives of the components of the displacement vector in Eulerian coordinates with respect to the Eulerian coordinates of the point.

In [5], it is proven that these derivatives are related by the continuity of the medium deformation through relationships, that in the notation of Fig. 10.3c, can be written for the plane x_1x_2,

$$\frac{\partial u_2}{\partial x_1} = \left(1 + \frac{\partial u_1}{\partial x_1}\right) \tan\theta_{12} \tag{10.31}$$

A similar equation can be obtained for the plane x_1-x_3,

$$\frac{\partial u_3}{\partial x_1} = \left(1 + \frac{\partial u_1}{\partial x_1}\right) \tan\theta_{13} \tag{10.32}$$

For x_2x_3 the equation is,

$$\frac{\partial u_3}{\partial x_2} = \left(1 + \frac{\partial u_2}{\partial x_2}\right) \tan\theta_{23} \tag{10.33}$$

All these derivatives can be computed utilizing the techniques outlined in [2] by differentiation in the frequency plane [6] without unwrapping the phase information.

10.6 Determination of Displacements and Strains of the Heart

As an illustration of the proposed approach to 3D displacement and strain determination, images generated by the Magnetic Image Resonance (MRI) method are utilized. MRI images are produced by "illuminating" the observed sample with an intense magnetic field. To this magnetic field, interrogating signals are applied in a temporal sequence that is required to obtain the magnetization information of the different voxels inside the observed object volume. What information is collected? Position of the voxels in the 3D space and the state of magnetization of the voxels. The state of magnetization depends on the chemical composition of the observed voxels thus though MRI it is possible to obtain information on the 3D spatial composition of the observed object. The magnetic resonance law depends on the changing spinning properties of protons in the nuclei of molecules and can only be observed in chemical elements that have different isotopes. An important property of magnetic resonance is the process of tagging the observed volume with planes that modulate periodically the intensity of the resulting image. The tagging planes are attached to the observed volume elements and create the system of reference illustrated in Figs. 10.1 and 10.2. The tagging process is a time-dependent phenomenon and fades away with time, thus limitations arise in the observation process of deformations. One should also realize that the functions of a camera and a sensor recorder in visible light are performed by hardware and software that generates an image output in levels of gray needed by the human observed to understand the content of the output of the MRI system.

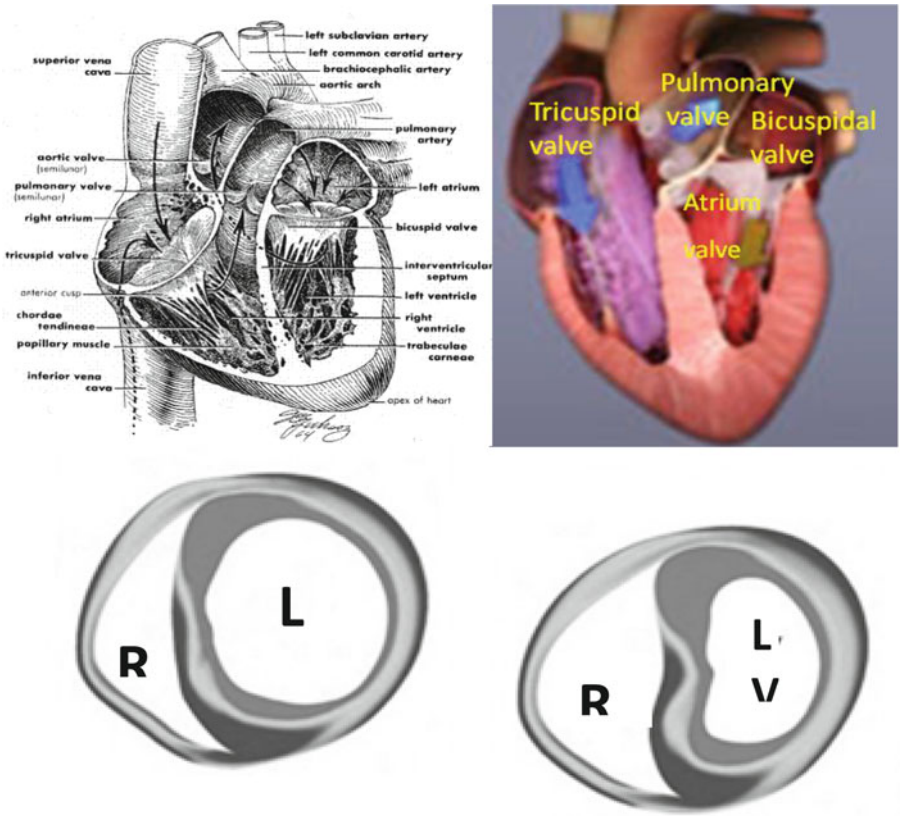

Fig. 10.9 Heart-long axis cross section (*top*) and short-axes cross sections (*bottom*)

To facilitate the understanding of the deformation analysis of the heart, it is necessary to provide a brief description of the heart anatomy, Fig. 10.9. The heart is a complex pumping system, consisting of two main vessels, right ventricle (RV), left ventricle (LV), a common wall, the septum. At the upper end of the ventricles are located valves controlling the inflow and outflow of blood regulated by electric signals. At each stage of the heart cycle the walls contract or expand to receive the blood inflow and to propel the blood output.

The composition of the heart is complex because it has muscles, veins, arteries, nerves and connecting tissues. For the deformation analysis, the Continuum Mechanics model is utilized and the continuum replaces the actual complex configuration of the heart. If the MRI is recorded from a leaving organism there are problems that must be solved. These problems are consequence of rigid body translations and rotations inherent in a leaving organism. The detailed description of the required correction of the observed images is beyond the scope of this paper. In the images analyzed corrections have been introduced.

Figure 10.10 shows tagged images of the RV and LV of a human heart, it shows the tagged images of the hearts' RV and LV in two subsequent times of the contraction period at mid-systole.

The corrections caused by rigid body motions have already been mentioned. The presence of the tagged lines on the images provided the necessary information to make small corrections for scale and rotation of the images. The reference tagging planes are captured at the instant of time that the heart begins to contract.

For data processing, digital moiré is applied and to get accurate values at boundaries of the ventricles fringe patterns are extended to the full field of view [8]. To complete the data processing [2], additional carrier lines are added to the image. Since the digital moiré is utilized, the fringes in the reference configuration provide the pitch "p" of the gratings utilizing to tag the images. It should be mentioned that orthogonal carriers are not present in the vertical plane, due to the time limitations imposed by the tagging process. As indicated before about Fig. 10.3, only one projection is required. Furthermore, as indicated in the analysis of the derivatives, the missing derivatives can be computed by the corresponding eqs.

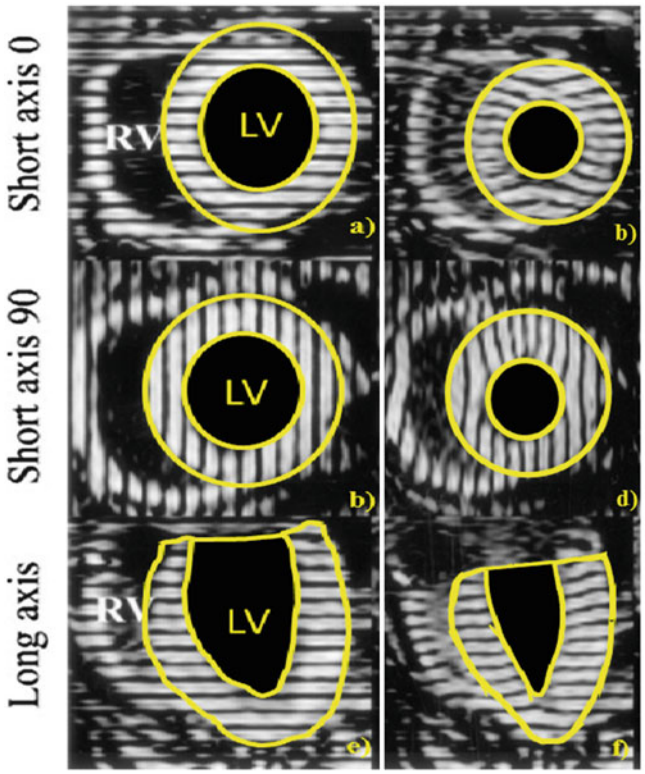

Fig. 10.10 Short-axis (0° and 90°) and long-axis MRI images of the right ventricle (RV) and left ventricle (LV). Reference configurations correspond to Fig. 10.9a, c, e (Images were taken from Ref. [7])

10.7 Processing of the Data Contained in MRI Tagged Images

Figure 10.11 illustrates the process of obtaining the displacements of the heart's left ventricle. In Fig. 10.11, one has the required grid lines patterns I_u that provide horizontal displacements; I_v that corresponds to the vertical displacements and I_{w1} that displays the out-of-plane displacements. Figure 10.10 shows the initial configuration. The components of the displacement $\mathbf{d}_p$ for a point P in the sections A-B and C-D are computed applying the following procedures. The projections of the vector $\mathbf{d}_p$ illustrated in Fig. 10.7, is the sum of u_1, u_2 and u_3. Each one of these components are obtained from the FTs' of the patterns I_u, I_v and I_{w1} along axes x_1, x_2 and x_3, respectively. Since the heart is contracting, the arrow direction indicates this fact by going towards P.

The maps of displacements u_1, u_2 and u_3 experienced by the left ventricle are shown in Fig. 10.12a–c. Values indicated by color maps are consistent with the sketch of Fig. 10.11.

10.8 Computation of the Strains

From the recorded images and performing the differentiations in the frequency space utilizing the wrapped phase pattern, the tensor of Eq. (10.30) is computed.

The lack of the orthogonal planes in Fig. 10.11e, f implies that some components of the J tensor are unknown, as shown in Eq. (10.34),

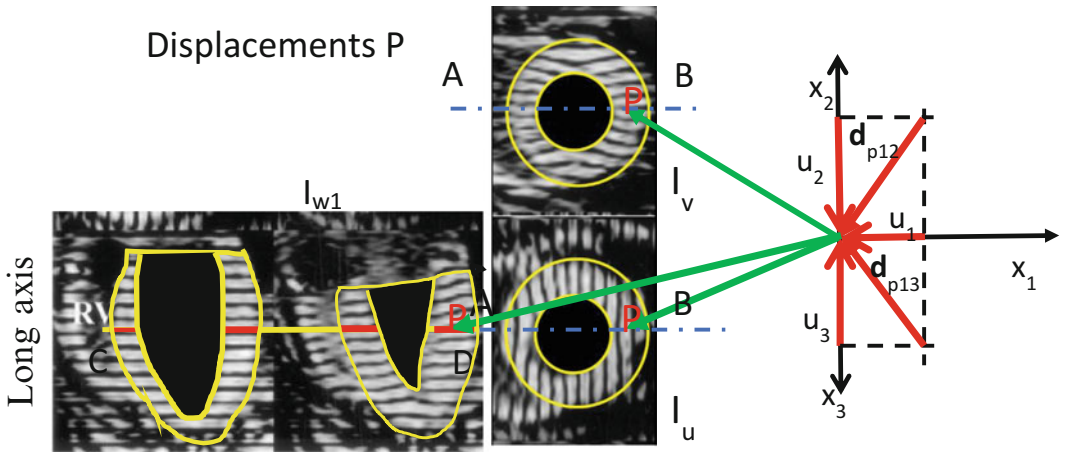

Fig. 10.11 The figure illustrates the process of retrieving the displacements components at a given point of the left ventricle. The vectors converge to the point P indicating compressive displacements

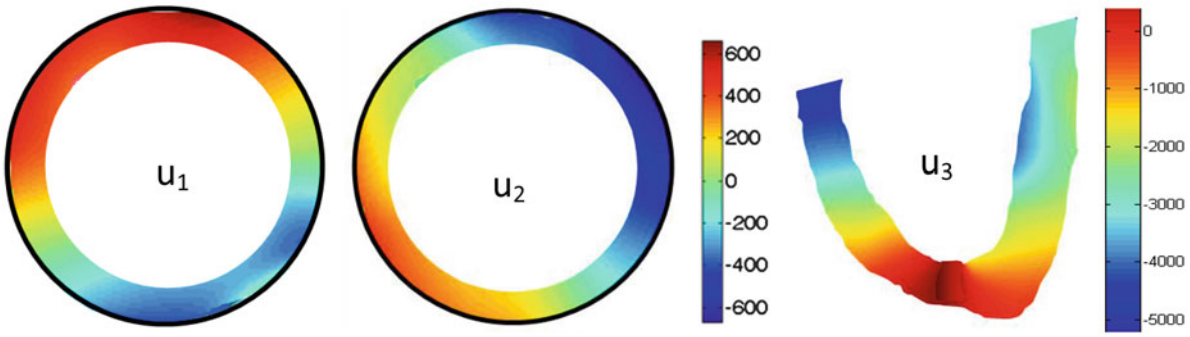

Fig. 10.12 Displacement components (expressed in μm) of the left ventricle

$$\mathrm{J} = \begin{bmatrix} \frac{\partial \mathrm{u}_1}{\partial \mathrm{x}_1} & \frac{\partial \mathrm{u}_1}{\partial \mathrm{x}_2} & X \\ \frac{\partial \mathrm{u}_2}{\partial \mathrm{x}_1} & \frac{\partial \mathrm{u}_2}{\partial \mathrm{x}_2} & X \\ X & X & \frac{\partial \mathrm{u}_3}{\partial \mathrm{x}_3} \end{bmatrix} \tag{10.34}$$

These missing derivatives are computed utilizing the relationships among derivatives.
After all the components of Eq. (10.34) are computed, the simplified Almansi strain tensor is obtained. For example,

$$\mathrm{e}^{\mathrm{E}}_{\mathrm{x}1} = \frac{\partial \mathrm{u}_1}{\partial x_1} - \frac{1}{2}\left[\left(\frac{\partial \mathrm{u}_1}{\partial \mathrm{x}_1}\right)^2 + \left(\frac{\partial \mathrm{u}_2}{\partial \mathrm{x}_1}\right)^2 + \left(\frac{\partial \mathrm{u}_3}{\partial \mathrm{x}_1}\right)^2\right] \tag{10.35}$$

$$\mathrm{e}^{\mathrm{E}}_{\mathrm{x}2} = \frac{\partial \mathrm{u}_2}{\partial \mathrm{x}_2} - \frac{1}{2}\left[\left(\frac{\partial \mathrm{u}_1}{\partial \mathrm{x}_2}\right)^2 + \left(\frac{\partial \mathrm{u}_2}{\partial \mathrm{x}_2}\right)^2 + \left(\frac{\partial \mathrm{u}_3}{\partial \mathrm{x}_2}\right)^2\right] \tag{10.36}$$

$$\mathrm{e}^{\mathrm{E}}_{\mathrm{x}3} = \frac{\partial \mathrm{u}_3}{\partial \mathrm{x}_3} - \frac{1}{2}\left[\left(\frac{\partial \mathrm{u}_1}{\partial \mathrm{x}_3}\right)^2 + \left(\frac{\partial \mathrm{u}_2}{\partial \mathrm{x}_3}\right)^2 + \left(\frac{\partial \mathrm{u}_3}{\partial \mathrm{x}_3}\right)^2\right] \tag{10.37}$$

Figure 10.13 shows the Eulerian components of the simplified Almansi strain tensor along the coordinate axis.

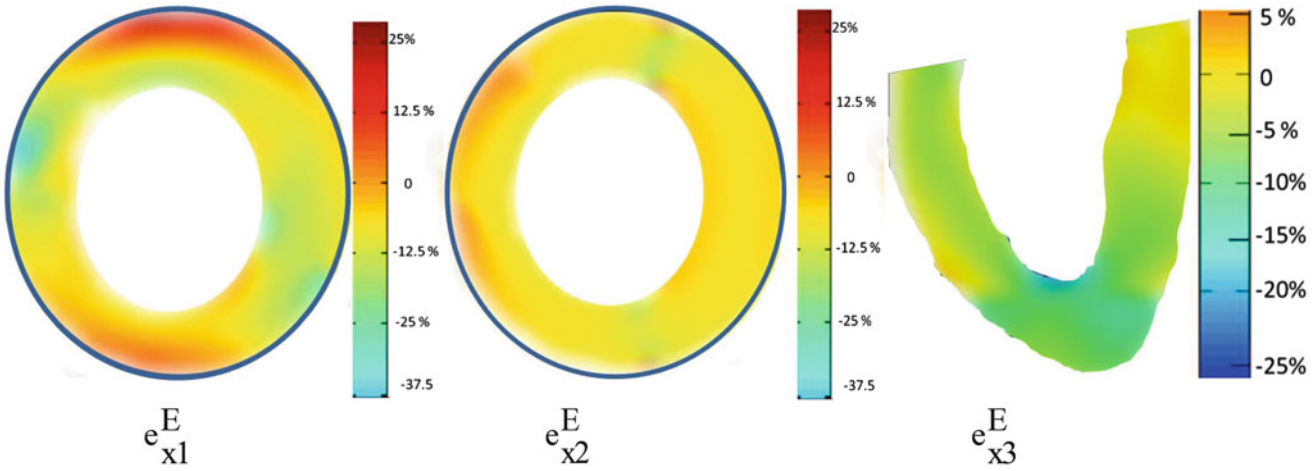

Fig. 10.13 Eulerian components of the strain tensor along coordinate axes

10.9 Discussion and Conclusions

Recently the authors have published papers [1, 2] about fringe pattern displacement information recovery. In these papers were addressed several aspects of fringe pattern processing that required additional analysis and developments to fully achieving the objective of a fast and accurate way of processing signals that contain displacement and deformation information in 2D.

The current paper deals with the generalization of the outlined procedures in 2D to 3D.

In [1], several fundamental aspects of fringe pattern analysis were dealt in the context of 1D signals. It is stressed that a fundamental concept of fringe pattern analysis is the concept of local phase. It is also pointed out that the definition of local phase in 1D requires the introduction of a 2D complex space that is geometrically represented by the unit circle.

In [2], it is shown that the concept of local phase in 2D requires a 3D complex space. Furthermore, it is indicated that the unit circle is replaced by a well-known geometrical surface utilized in Photoelasticity to represent the different states of polarization of light, the Poincare sphere. Thus, the use of the Poincare is extended to patterns associated with displacements and metrological signals, a geometrical illustration of the concept of monogenic phasor. The current paper extends the concept of monogenic function to fringe patterns that correspond to 3D displacements. The addition of one dimension leads to a hyper-4D complex space and to a 4D hyper-sphere. The components of the radius of the 4D sphere are derived. The process of computing the components is illustrated with examples. An application to images produced by the MRI process applied to a human heart left ventricle provides the actual application of the theoretical developments yielding 3D displacements and displacement derivatives. The additional steps of the generalization of the monogenic phasor to the different dimensions are not trivial. Each one of the process of generalization required additional procedures that provided different aspects of the more general problem. For example, the 3D displacements case was handled by introducing a multi-dimensional generalization of the Fourier Transform that deals with vectorial quantities and has very interesting properties that are utilized practically in the process of data retrieval.

The fact that the FT, the Hilbert transform and the Radon transform are connected to each other, opens new avenues for further future developments in the actual study of 3D deformations.

References

1. Sciammarella, C.A., Lamberti, L.: Mathematical models utilized in the retrieval of displacement information encoded in fringe patterns. Opt. Lasers Eng. **77**, 100–111 (2016)
2. Sciammarella, C.A., Lamberti, L.: Generalization of the Poincare sphere to process 2D displacement signals. Opt. Lasers Eng. **93**, 114–127 (2017)
3. Fourier analysis for vectors. http: www.uio.no/studier/emner/matnat/math/MAT-INF2360/v12/fouriervectors

4. Ciattoni, A., Crosignani, B., Di Portoab, P.: Vectorial free-space optical propagation: a simple approach for generating all-order nonparaxial corrections. Opt. Commun. **177**, 9–13 (2000)
5. Sciammarella, C.A., Lamberti, L.: Basic models supporting experimental mechanics of deformations, geometrical representations, connections among different techniques. Meccanica. **50**, 367–387 (2015)
6. Sciammarella, C.A., Narayanan, R.: The determination of the components of the strain tensor in holographic interferometry. Exp. Mech. **24**, 257–264 (1984)
7. Wyman, B.T., Hunter, W.C., Prinzen, F.W., McVeigh, E.R.: Mapping propagation of mechanical activation in the paced heart with MRI tagging. Am. J. Physiol. Heart Circ. Physiol. **276**(3), H881–H891 (1999)
8. Sciammarella, C.A., Sciammarella, F.: Experimental Solid Mechanics. John Wiley and Sons, Chichester (2012)

Prof. Cesar Sciammarella was the Director of the world renowned Experimental Mechanics Laboratory at the Illinois Tech. for more than 30 years. He has received the Theocaris, Hetenyi, Lazan, and Frocht Awards, the William M. Murray Medal and the Honorary Membership of SEM. He received the Fylde Electronics Prize in 2010. He authored more than 200 technical papers.